










Thermochemical structure and evolution of cratonic lithosphere in central and southern Africa

Juan C. Afonso^{1,2} , Walid Ben-Mansour^{2,3}, Suzanne Y. O'Reilly², William L. Griffin², Farshad Salajegheh², Stephen Foley², Graham Begg², Kate Selway⁴ , Andrew Macdonald⁵ , Nicole Januszcak⁶ , Ilya Fomin² , Andrew A. Nyblade⁷  and Yingjie Yang⁸ 

The thermochemical structure of the subcontinental mantle holds information on its origin and evolution that can inform energy and mineral exploration strategies, natural hazard mitigation and evolutionary models of Earth. However, imaging the fine-scale thermochemical structure of continental lithosphere remains a major challenge. Here we combine multiple land and satellite datasets via thermodynamically constrained inversions to obtain a high-resolution thermochemical model of central and southern Africa. Results reveal diverse structures and compositions for cratons, indicating distinct evolutions and responses to geodynamic processes. While much of the Kaapvaal lithosphere retained its cratonic features, the western Angolan-Kasai Shield and the Rehoboth Block have lost their cratonic keels. The lithosphere of the Congo Craton has been affected by metasomatism, increasing its density and inducing its conspicuous low-topography, geoid and magnetic anomalies. Our results reconcile mantle structure with the causes and location of volcanism within and around the Tanzanian Craton, whereas the absence of volcanism towards the north is due to local asthenospheric downwellings, not to a previously proposed lithospheric root connecting with the Congo Craton. Our study offers improved integration of mantle structure, magmatism and the evolution and destruction of cratonic lithosphere, and lays the groundwork for future lithospheric evolutionary models and exploration frameworks for Earth and other terrestrial planets.

The thermochemical structure of the lithosphere exerts important controls on the localization of seismic activity, magmatism and giant ore deposits^{1–3}. Information on lithosphere-scale structure is rapidly becoming an important component of modern exploration and hazard-mitigation frameworks^{1,4–7}. It is also essential to understanding the origin, evolution and destruction of cratons and the physico-chemical interactions between the lithosphere and the sublithospheric mantle.

Despite its fundamental importance, imaging the fine-scale thermochemical structure of the lithosphere from geophysical data has proved difficult. While temperatures obtained from different methods broadly agree, the simultaneous characterization of the mineralogical and major-element chemical structure (essential for resource exploration) from geophysical data is considerably more complex and enigmatic^{8–13}. Consequently, the analysis of mantle samples (xenoliths and xenocrysts) brought to the surface by volcanoes is still considered the only reliable approach. Such samples, however, are scattered in space and time, and the interpolations needed for regional-scale predictive models involve large and unquantifiable uncertainties.

In this Article, we demonstrate an approach that integrates high-resolution land and satellite geophysical datasets and that offers a salient and viable alternative to interpolations of mantle samples. This is due to the more regular coverage and improved sensitivity to the thermochemical structure of the lithosphere that results from exploiting the complementary nature of these

datasets^{11–13}. We demonstrate the value of this approach using a probabilistic joint inversion method that fuses multiple geophysical datasets with the sensitivities required to image the thermal and compositional structures of the lithosphere and sublithospheric upper mantle (Methods). We focus on central and southern Africa, a region that encapsulates 3.5 billion years of evolution and hosts the Kalahari, Tanzanian and Congo cratons and a number of microcontinental cratonic blocks (for example, Kaapvaal, Zimbabwe, Angola and Bangweulu). This region is an excellent natural laboratory to probe fundamental questions about craton evolution, not only due to the large extent of cratonic lithosphere, but also because some domains have been affected by convergent margin and/or mantle plume activity with different impacts on thermochemical structure¹⁴, while others have not. It also supplied abundant xenolith-derived datasets that provide groundtruthing for the joint inversion approach used here.

We combined broadband seismic data from 870 stations in the study region with global and regional surface-wave data to obtain a high-resolution, consistent dataset of Rayleigh-wave dispersion curves (Methods). Geoid and gravity anomalies, elevation, surface heat flow and gravity gradients were also used in our inversion. The spatial resolution and complementary sensitivities of these datasets to bulk density and shear-wave velocity allow us to image the thermochemical structure of the central-south African lithosphere with unprecedented resolution and confidence.

¹Faculty of Geo-Information Science and Earth Observation (ITC), University of Twente, Enschede, Netherlands. ²ARC Centre of Excellence for Core to Crust Fluid Systems (CCFS), Macquarie University, North Ryde, New South Wales, Australia. ³Department of Earth and Planetary Sciences, Washington University, St Louis, MO, USA. ⁴Future Industries Institute, University of South Australia, Mawson Lakes, South Australia, Australia. ⁵De Beers Group Services, Johannesburg, South Africa. ⁶BHP Technical Centre of Excellence, Perth, Western Australia, Australia. ⁷Department of Geosciences, Pennsylvania State University, State College, PA, USA. ⁸Department of Earth and Space Sciences, Southern University of Science and Technology Shenzhen, Guangdong, China. ✉e-mail: j.c.afonso@utwente.nl

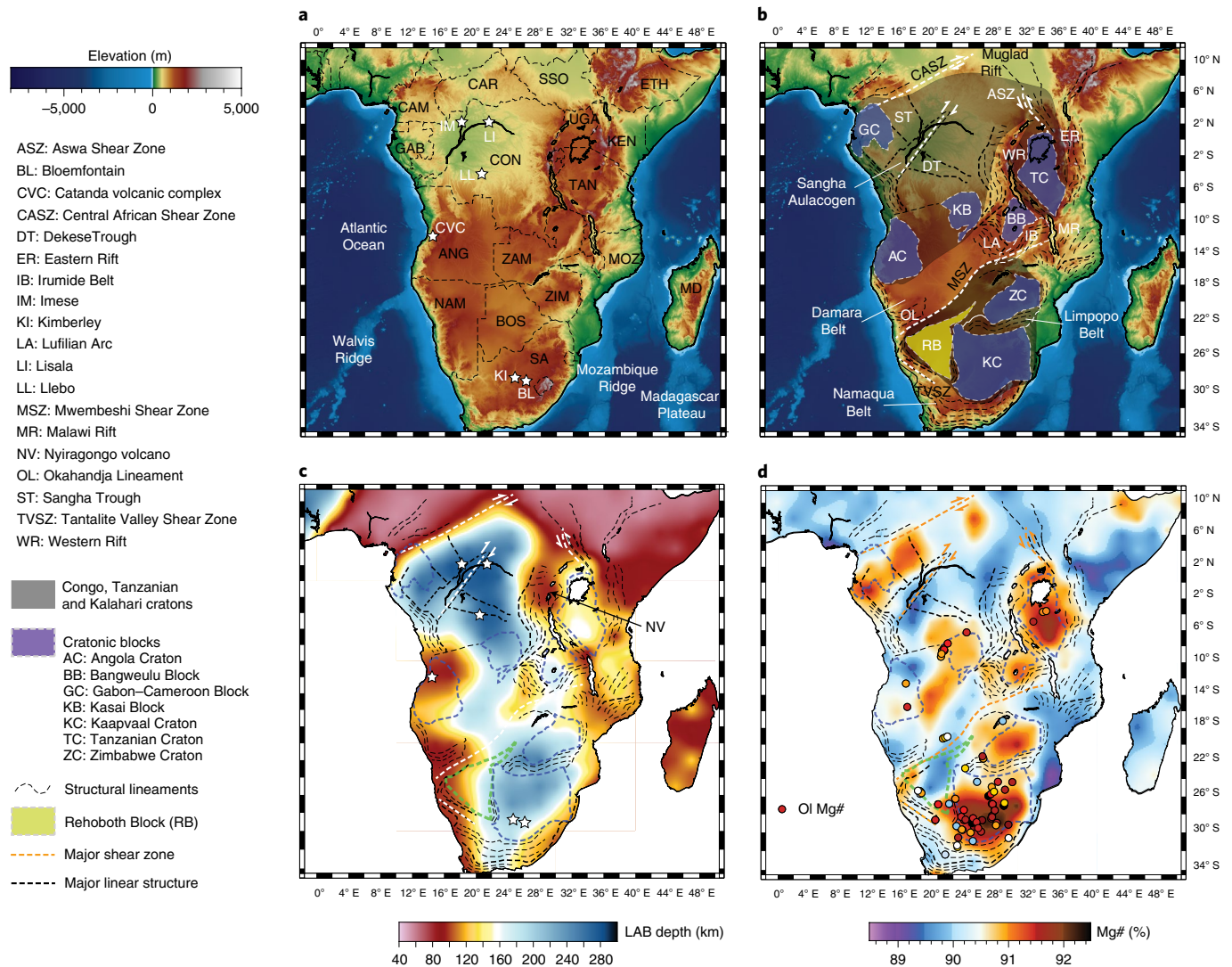


Fig. 1 | Tectonic and thermochemical structures in central and southern Africa. a, Map of the study region; black text indicates abbreviations of country names (ANG, Angola; BOS, Botswana; CAM, Cameroon; CAR, Central Africa Republic; CON, Democratic Republic of the Congo; ETH, Ethiopia; GAB, Gabon; KEN, Kenya; MD, Madagascar; MOZ, Mozambique; NAM, Namibia; SA, South Africa; SSO, South Sudan; TAN, Tanzania; UGA, Uganda; ZAM, Zambia; ZIM, Zimbabwe). White stars indicate localities mentioned in the text. **b**, Cratons, Precambrian blocks and other relevant tectonic features. **c**, Depth to the LAB, here taken as the depth to the 1,250 °C isotherm; major tectonic domains/features are also shown. **d**, Average Mg# (Mg/(Mg + Fe²⁺)) in the lithospheric mantle as constrained in **c**, with Mg# in olivine from mantle xenoliths reported in the literature.

Lithospheric thermochemical structure

Tomographic studies have highlighted a correlation between the extents of cratonic domains inferred by crustal elements and high mantle wavespeeds^{15–17}, suggesting that cratonic crust and the underlying lithospheric mantle root remain coupled through time. Our results indicate that this is not always the case (Fig. 1). The extent of anomalously thick lithosphere in central and southern Africa is smaller than that inferred from surface geology, requiring mechanisms that can erode/destroy the lithospheric mantle without affecting the crust, as suggested by recent high-resolution tomography¹⁸.

Our derived lithospheric structure exhibits a clear correlation with well-known mid- and large-scale surface structures. This is particularly evident in the East African Rift, the Central Africa Shear Zone (CASZ), the Okahandja Lineament/Mwembeshi Shear Zone and the boundaries of the Lufilian Arc (Supplementary Fig. 13). The CASZ is one of the largest shear zones in the continent; according to our results, it marks one of the largest steps in the lithosphere–asthenosphere boundary (LAB) globally: an ~200 km change in

lithospheric thickness over a distance of ~600 km. Notably, one of the world's largest magnetic anomalies, the enigmatic Bangui anomaly, is located in this region and is aligned with the imaged thermochemical structure (Supplementary Fig. 15).

On the Atlantic margin, marked lithospheric thinning occurs along the Damara Belt in Namibia and in the 'cratonic' interior of Angola. In both cases, crustal thinning is also apparent, suggesting that a common tectonic process affected both the crust and the lithospheric mantle. This is consistent with major extensional/transensional structures that developed in these two regions during the initial opening of the Atlantic Ocean¹⁹. Our predicted LAB depth beneath Namibia coincides well with a strong and widespread negative conversion at ~80 km (ref. 20), originally interpreted as a mid-lithosphere discontinuity within a 200-km-thick lithosphere²⁰. Our results indicate that this conversion instead represents the LAB.

In western Angola, a comparison between thermobarometry-based geotherms and our model reveals >80 km thinning of the lithosphere (Supplementary Fig. 16) since kimberlite emplacement

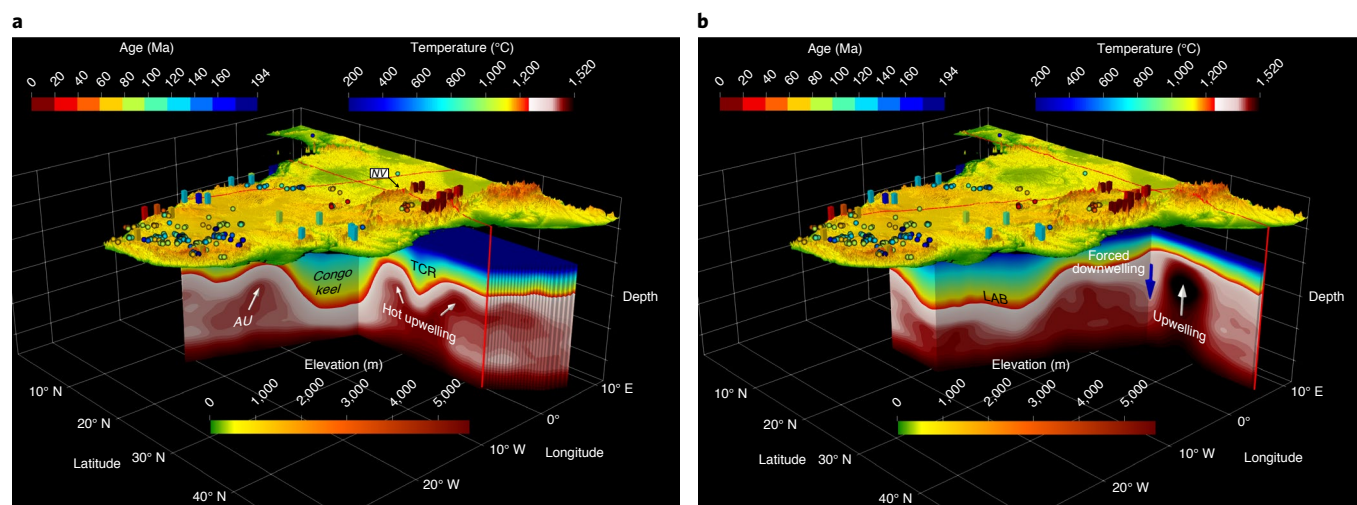


Fig. 2 | Three-dimensional renderings of the thermal structure beneath the study area. The eruption ages of kimberlitic and carbonatitic volcanism are indicated with coloured spheres and boxes, respectively. The surface projections of the vertical cross sections are indicated by the red lines over the topography. **a**, A hot upwelling beneath the Tanzanian Craton (TCR) impinges on the LAB and diverts towards its sides, focusing shallow decompression melting along the western and eastern branches of the East Africa Rift. In addition to the young volcanism along the edges of the craton, Quaternary kimberlitic volcanism generated at depths >150 km (ref. ³²) occurred in the middle of the craton, above the high-temperature anomaly (NV, Nyiragongo volcano). A smaller temperature anomaly, probably associated with a sublithospheric upwelling, is visible beneath Angola (AU). **b**, A forced sublithospheric downwelling towards the north of the Tanzanian Craton, which precludes the generation of decompression melting in the mantle, results from the mechanical interaction between the large Afar upwelling and the adjacent lithospheric structure.

(216–252 million years ago (Ma) (ref. ²¹)). Eruption ages and those of major crustal structures are consistent with whole-of-lithosphere thinning during the opening of the Atlantic Ocean, with the Tristan Plume probably contributing to the weakening and thinning of the lithospheric mantle. Carbonate-rich ultramafic lavas <1 Myr old in Angola's Catanda volcanic complex²² have been interpreted to originate from local mantle upwelling beneath thinned lithosphere²², but the nature and size of the upwelling and the LAB depth were poorly constrained. Our results confirm significant thinning of the lithosphere beneath this region (Fig. 1), but also reveal a hot anomaly in the shallow sublithospheric upper mantle (Fig. 2a), which may explain the carbonatitic and alkaline magmatism in Angola and the recent uplift of the Bie Dome. Another clear correlation between thin lithosphere and thin crust is observed along the western and eastern branches of the East Africa Rift (Figs. 1 and 3), again suggesting whole-of-lithosphere thinning. Although localized lithospheric thinning beneath the Malawi Rift is not discernible in previous large-scale LAB models (Supplementary Fig. 13), it has been imaged in high-resolution studies²³.

A key feature of our model is a thermochemical anomaly coincident with the Lufilian Arc and its extension into the eastern branch of the Damara Belt (Fig. 1). These two large-scale structures were created during collision of the Kalahari and Congo cratons in the early Palaeozoic. Before the collision, both regions experienced widespread extension, producing a failed intracontinental rift in the Lufilian Arc and a marginal oceanic basin in the Damara Belt. Our results show a domain of relatively fertile mantle along the Damara–Katanga belts (Fig. 1), consistent with both belts experiencing multiple periods of collisional orogenesis, rifting and mafic–ultramafic magmatism in the Proterozoic. The net result is that the lithospheric mantle of both zones is thinned and likely to be strongly refertilized. While a coherent mantle compositional anomaly is observed along the Damara and Lufilian domains, the LAB is conspicuously shallow beneath the Lufilian Arc. Its northern boundary is particularly well defined, separating the arc domain from the Congo Craton (Fig. 1).

Cratonic domains

Comparing our thermochemical maps and the cratonic domains inferred by surface geology reveals both striking correlations and discrepancies. The Kaapvaal and Zimbabwe cratons are clearly identified in our model; both exhibit a relatively thick and highly depleted lithospheric mantle despite having been affected by plume activity and volcanism for at least 2,000 Myr (Large Igneous Provinces: 2,055 Ma Bushveld, 1,105 Ma Umkondo and ~180 Ma Karoo). This is also true for the region around Kimberley and Bloemfontein (Fig. 1c,d), which still retains a depleted and relatively thick lithosphere (170–200 km).

A corridor of more fertile mantle between the Kaapvaal and Zimbabwe cratons coincides broadly with the Limpopo Belt. The region affected by Bushveld–Molopo Farms magmatism within the Kaapvaal Craton also shows a more fertile composition, consistent with xenolith evidence²⁴. The compositional structure retrieved by our inversion across the Kaapvaal Craton is in excellent agreement with that inferred from a regional study of mantle samples from 29 kimberlites²⁵ (105–70 Ma; Supplementary Fig. 17 and Fig. 1d). These independent validations are particularly important because our inversion is driven entirely by geophysical data, with no input from local xenolith information.

The Tanzanian Craton is visible in our model as a region of highly depleted lithospheric mantle and relatively thick lithosphere (~150–200 km), bounded by the branches of the East African Rift. The most depleted areas include localities where xenoliths/xenocrysts confirm highly refractory lithosphere (for example, Igwisi, Mwadui and Nzega on the craton and Labait on the craton margin). The map of Mg# (MgO/(FeO + MgO); Fig. 1) shows a clear separation between the Tanzanian Craton and the Proterozoic Bangweulu Block in the south. We do not see the previously proposed¹⁸ deep cratonic root beneath the southern Irumide Belt (Niassa Craton). Although we obtain relatively high velocities in the mantle, the joint fit of all observables favours a small-scale sublithospheric downwelling rather than a thick lithospheric root (Supplementary Fig. 19). Since this orogenic belt experienced Mesoproterozoic

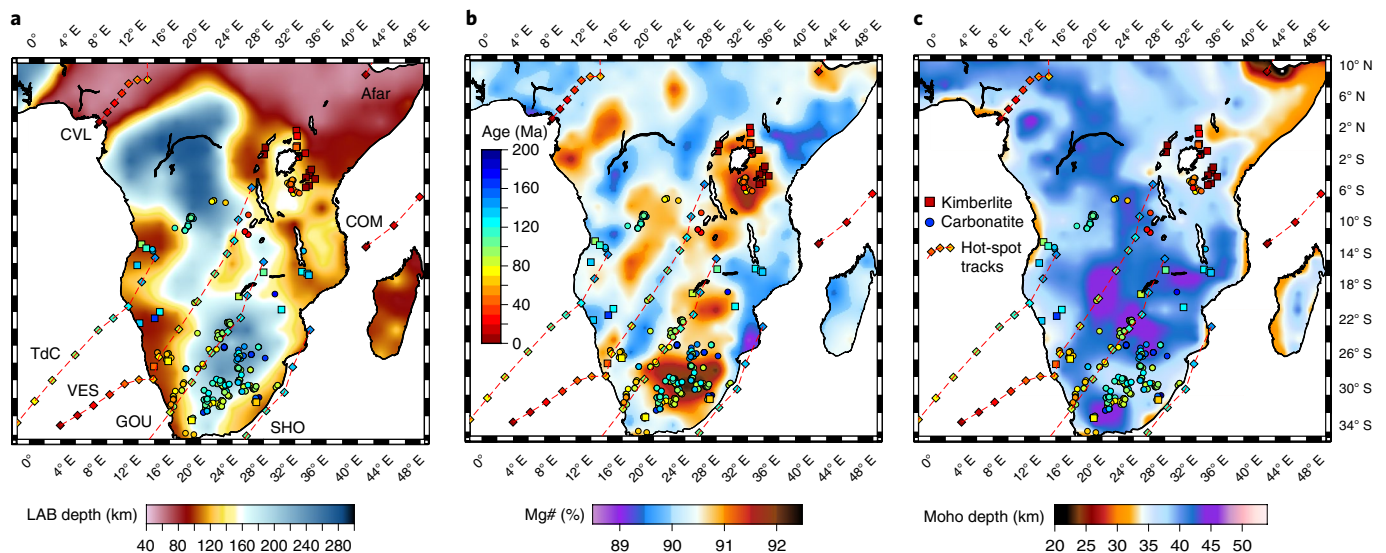


Fig. 3 | Hot-spot tracks and location of kimberlitic and carbonatitic volcanism superimposed on lithospheric structure. a, Depth to the LAB. COM, Comores; CVL, Cameroon volcanic line; GOU, Gough; SHO, Shona; TdC, Tristan da Cunha; VES, Vesma. **b**, Average composition of the lithospheric mantle (as Mg#). **c**, Moho depth. Locations of kimberlite (circles) and carbonatitic (squares) volcanics with reliable ages (colour scale) are shown. Hot-spot tracks (from ref. ¹⁴) are denoted by dashed lines and diamonds; their colours represent the age at which the hot spot was at that location.

convergence (including arc magmatism) and collision, Pan-African, Palaeozoic and Tertiary thermal reworking and extensional tectonics²⁶, it seems unlikely that its lithospheric mantle would retain cratonic characteristics. This highlights an important limitation of using seismic velocities alone to derive models of the LAB^{13,27}. In regions where convective downwellings occur, the seismically derived LAB will be overestimated due to the lack of sensitivity in separating convective from non-convective anomalies. That is, cold sublithospheric mantle in small-scale downwellings may be mistakenly interpreted as ancient cratonic roots.

Towards the north, the Tanzanian Craton extends to the boundary between Uganda and South Sudan; this is visible in both the Mg# and LAB maps (Fig. 1). An important observation is that the Tanzanian and Congo cratons do not seem connected by a thick lithospheric ‘bridge’ along and around the Aswa transform, as inferred from surface geology²⁸ and from the observation that carbonatitic magmatism on the western side of the Tanzanian Craton stops towards the north²⁹. Our model offers an alternative explanation. Figure 2a shows a large asthenospheric upwelling beneath the Tanzanian Craton (linked to the Afar upwelling to the north); it branches off where it impinges on the root of the craton, also contributing to its high elevation. This results in asthenospheric material being focused towards the Western and Eastern rifts, where it reaches the shallower depths required to produce carbonatitic melts. By contrast, the asthenosphere towards the north participates in a forced downwelling triggered by the interaction between the adjacent Afar upwelling (Fig. 2b) and the surrounding lithospheric structure. Although the LAB in this region is relatively shallow (~100 km), the local asthenospheric circulation impedes decompression melting. In the central part of the craton, kimberlitic magma generated at depths >150 km has erupted during the Quaternary³⁰ (Figs. 2 and 3), supporting this geodynamic scenario and our LAB estimates.

The lithosphere of the Congo Craton shows some striking and unexpected features. Its deepest roots, near the localities of Imese, Lisala and Llebo, extend below 260 km (Fig. 1). The eastern edge has been eroded considerably, forming a narrow corridor that focuses shallow asthenospheric upwellings (Figs. 1c and 2a). Similarly, the middle and western portions of the Angolan Shield have been

thinned by at least 80 km since the intrusion of Triassic kimberlites (see the preceding and Supplementary Fig. 16). Northwards, the Congo Craton is bounded by two major shear zones: the CASZ and the (inferred) northern continuation of the Aswa Shear Zone. The correlation between these shear zones and the sharp boundary of the craton suggests that the entire lithosphere has participated in strike-slip deformation and that such structures exerted a dominant role in the evolution of the LAB.

A modest thinning of the lithosphere propagates from northern Angola into the Kenge and Bandunu regions in Congo (Fig. 1). This feature coincides roughly with a compositional anomaly in the lithospheric mantle (Fig. 1) and with the junction of two important, long-lived transtensional structures: the Shangha Aulacogen and the Dekese Trough³¹. The southwest–northeast-trending compositional anomaly dissects the Congo Craton, otherwise characterized by strongly to moderately depleted mantle, and joins a second anomaly along the eastern margin of the craton.

The thermochemical structure of the Congo Craton imaged here reconciles long-standing questions about the origin of the Congo Basin and the associated gravity/geoid anomaly. A late Neoproterozoic rift origin for the basin, followed by a long period (>560 Myr) of thermal relaxation, has been proposed on the basis of subsidence curves, stratigraphy and structural features of the basin^{32,33}. Others have proposed that most of the subsidence reflects a downwelling in the sublithospheric mantle³⁴. This downwelling would not affect lithospheric mantle composition, whereas rifting usually does. Indeed, there is abundant evidence of magmatism associated with extensional episodes³³. Since the mantle compositional anomalies are spatially correlated with regions of known extension and magmatism in the craton, we suggest that the original depleted mantle root of the Congo Craton was refertilized during episodes of extension, increasing its density and thinning it locally. This assigns a clear meaning to the postulated need for a high-density anomaly within the lithospheric mantle³⁵ and resolves the problem³² of a thick and strongly depleted mantle root explaining both the gravity anomalies and the subsidence/topography. Although we cannot confidently constrain the chemical stratification of the lithospheric mantle, additional inversions (Supplementary Fig. 20) show only a slight preference for more depleted material at shallower depths.

Last, we note that the LAB geometry surrounding and beneath the Congo Craton represents an ideal setting for the nucleation of gravitational instabilities in the asthenosphere, consistent with evidence from earthquake focal mechanisms and seismic tomography^{3,36}. If downwellings nucleate beneath the Congo Craton, a dynamic effect would be seen in the topography and would have played a role in the recent subsidence history of the basin^{32,35}. However, additional tests (Supplementary Fig. 21) demonstrate that our results are robust against dynamic effects.

Implications for the evolution of cratonic lithosphere

Our study shows that the Tanzanian, Zimbabwe, Kaapvaal and Bangweulu cratons/blocks have retained depleted compositions and relatively thick lithospheres in their cores. The Congo Craton, however, experienced extensive refertilization during extension across the middle of the Congo basin (Fig. 1 and Supplementary Fig. 17). Despite this, it remained a coherent block between two greatly thinned regions (CASZ and Angola), suggesting that any modification/thinning of the lithosphere beneath the Congo Basin was thermally/mechanically recovered by the time the Atlantic Ocean started opening³². This is likely given the recovery time following the Precambrian rifting and the tendency of thick roots to nucleate cold downwellings, which further favour lithospheric cooling. In addition, no known plumes have affected this region in the past 300 Myr. Therefore, it is possible that the combined influence of the Tristan Plume and the already weakened and thinned CASZ preferentially localized upwellings and deformation beneath Angola and Cameroon, leaving the region between them affected only by slight compression due to return downwellings in the asthenosphere.

Another important contrast in cratonic behaviour is exemplified by the differences between the Kaapvaal Craton and the southern margins of the Congo Craton. Hot-spot reconstructions indicate that the Kaapvaal experienced multiple episodes of plume activity (Fig. 3). Although there is evidence for lithospheric erosion by plumes¹⁸ (Fig. 3), our results show that most of the Kaapvaal Craton has preserved a highly depleted and thick lithosphere with a coherent core. By contrast, the western parts of the Angolan–Kasai Shield and the Rehoboth Block have lost their thick depleted keels. These regions, together with the eastern portions of the Damara Belt, have been affected not only by plumes (Fig. 3) but also by Proterozoic convergent events and transtensional tectonics (except the Rehoboth Block) during the break-up of Pangaea. It has been argued¹⁴ that the lower part of the Kaapvaal root was completely delaminated in the Cretaceous and replaced by cooled asthenospheric mantle. This is contradicted by Re–Os data for both xenoliths and sulfide grains from late Cretaceous kimberlites; Archaean model ages are found throughout the lithospheric column, in both depleted and metasomatized samples³⁷. Notwithstanding this, the correlation of hot-spot tracks with regions of refertilized mantle and kimberlitic volcanism (Fig. 3b) suggests a genetic link.

A pattern emerges from the evidence discussed. Cratons share a number of features inherited from their formation/stabilization³⁸, but their evolution and present-day thermochemical structure can differ remarkably depending on various geodynamic factors. Foremost among these are the presence of pre-existing weak zones in the lithosphere (for example, past subduction zones, orogens and shear zones), the physico-chemical interaction between upwellings and lithospheric architecture, and the large-scale stress field. Pre-existing zones of weakness play a critical role in combination with mantle upwellings during continental break-up³⁹, and studies of interactions between asthenospheric flow and craton geometry suggest that sharp craton margins, such as that imaged around the CASZ, are more resistant to deformation and erosion than gradual margins (for example, Rehoboth Block)⁴⁰.

The improved ability to map the fine-scale thermochemical structure of the lithosphere and upper mantle provides a new

integrative template for linking, validating and interpreting information from geochemical, geophysical and geodynamic studies. By harnessing land and satellite geophysical observations, our approach replicates detailed information from mantle xenoliths and therefore confidently extends the imaging to regions without xenolith data. We expect this approach to contribute to the development of next-generation planetary models and exploration strategies.

Online content

Any methods, additional references, Nature Research reporting summaries, source data, extended data, supplementary information, acknowledgements, peer review information; details of author contributions and competing interests; and statements of data and code availability are available at <https://doi.org/10.1038/s41561-022-00929-y>.

Received: 9 July 2021; Accepted: 8 March 2022;

Published online: 18 April 2022

References

- Griffin, W., Begg, G. & O'Reilly, S. Continental-root control on the genesis of magmatic ore deposits. *Nat. Geosci.* **6**, 905–910 (2013).
- Holwell, D. A. et al. A metasomatized lithospheric mantle control on the metallogenic signature of post-subduction magmatism. *Nat. Commun.* **10**, 3511 (2019).
- Craig, T. J., Jackson, J. A., Priestley, K. & McKenzie, D. Earthquake distribution patterns in Africa: their relationship to variations in lithospheric and geological structure, and their rheological implications. *Geophys. J. Int.* **185**, 403–434 (2011).
- Hoggard, M. J. et al. Global distribution of sediment-hosted metals controlled by craton edge stability. *Nat. Geosci.* **13**, 504–510 (2020).
- Begg, G. G., Hronsky, J. M. A., Griffin, W. L. & O'Reilly, S. Y. in *Processes and Ore Deposits of Ultramafic-Mafic Magmas Through Space and Time* (eds Mondal, S. K. & Griffin, W. L.) 1–46 (Elsevier, 2018).
- Heinson, G. et al. The crustal geophysical signature of a world-class magmatic mineral system. *Sci. Rep.* **8**, 10608 (2018).
- Begg, G. et al. Lithospheric, cratonic, and geodynamic setting of Ni–Cu–PGE sulfide deposits. *Econ. Geol.* **105**, 1057–1070 (2010).
- Schutt, D. L. & Leshner, C. E. Effects of melt depletion on the density and seismic velocity of garnet and spinel lherzolite. *J. Geophys. Res.* **111**, B05401 (2006).
- O'Reilly, S. Y. & Griffin, W. L. Imaging chemical and thermal heterogeneity in the sub-continental lithospheric mantle with garnets and xenoliths: geophysical implications. *Tectonophysics* **416**, 289–309 (2006).
- Afonso, J. C. et al. On the Vp/Vs–Mg# correlation in mantle peridotites: implications for the identification of thermal and compositional anomalies in the upper mantle. *Earth Planet. Sci. Lett.* **289**, 606–618 (2010).
- Afonso, J. C. et al. 3-D multi-observable probabilistic inversion for the compositional and thermal structure of the lithosphere and upper mantle. I: A priori petrological information and geophysical observables. *J. Geophys. Res. Solid Earth* **118**, 2586–2617 (2013).
- Afonso, J. C., Fullea, J., Yang, Y., Connolly, J. A. D. & Jones, A. G. 3-D multi-observable probabilistic inversion for the compositional and thermal structure of the lithosphere and upper mantle. II: General methodology and resolution analysis. *J. Geophys. Res. Solid Earth* **118**, 1650–1676 (2013).
- Afonso, J. C. et al. 3-D multiobservable probabilistic inversion for the compositional and thermal structure of the lithosphere and upper mantle: III. Thermochemical tomography in the Western-Central US. *J. Geophys. Res. Solid Earth* **121**, 7337–7370 (2016).
- Hu, J. et al. Modification of the Western Gondwana Craton by plume–lithosphere interaction. *Nat. Geosci.* **11**, 203–210 (2018).
- Grand, S. Mantle shear-wave tomography and the fate of subducted slabs. *Phil. Trans. R. Soc. A* **360**, 2475–2491 (2002).
- Ritsema, J. & Van Heijst, H. J. Seismic imaging of structural heterogeneity in Earth's mantle: evidence for large-scale mantle flow. *Sci. Prog.* **83**, 243–259 (2000).
- Fishwick, S. Surface wave tomography: imaging of the lithosphere–asthenosphere boundary beneath central and southern Africa? *Lithos* **120**, 63–73 (2010).
- Celli, N. L. et al. African cratonic lithosphere carved by mantle plumes. *Nat. Commun.* **11**, 92 (2020).
- Torsvik, T. H., Rousse, S., Labails, C. & Smethurst, M. A. A new scheme for the opening of the South Atlantic Ocean and the dissection of an Aptian salt basin. *Geophys. J. Int.* **177**, 1315–1333 (2009).
- Yuan, X. et al. Seismic structure of the lithosphere beneath NW Namibia: impact of the Tristan da Cunha mantle plume. *Geochem. Geophys. Geosyst.* **18**, 125–141 (2017).

21. Jelsma, H. et al. Kimberlites from central Angola: a case study of exploration findings. In *Proc. 10th International Kimberlite Conference* (eds Pearson, G. D. et al.) 173–190 (Springer, 2012).
 22. Giuliani, A. et al. Southwestern Africa on the burner: Pleistocene carbonatite volcanism linked to deep mantle upwelling in Angola. *Geology* **45**, 971–974 (2017).
 23. Hopper, E. et al. Preferential localized thinning of lithospheric mantle in the melt-poor Malawi Rift. *Nat. Geosci.* **13**, 584–589 (2020).
 24. Hoal, K. E. O. Samples of Proterozoic Fe-enriched mantle from the Premier kimberlite. *Lithos* **71**, 259–272 (2003).
 25. Kobussen, A. F., Griffin, W. L. & O'Reilly, S. Y. Cretaceous thermo-chemical modification of the Kaapvaal cratonic lithosphere, South Africa. *Lithos* **112**, 886–895 (2009).
 26. Fritz, H. et al. Orogen styles in the East African Orogen: a review of the Neoproterozoic to Cambrian tectonic evolution. *J. Afr. Earth Sci.* **86**, 65–106 (2013).
 27. Eaton, D. W. et al. The elusive lithosphere–asthenosphere boundary (LAB) beneath cratons. *Lithos* **109**, 1–22 (2009).
 28. Link, K. et al. Continuous cratonic crust between the Congo and Tanzania blocks in western Uganda. *Int. J. Earth Sci.* **99**, 1559–1573 (2010).
 29. Rosenthal, A., Foley, S. F., Pearson, D. G., Nowell, G. M. & Tappe, S. Magmatic evolution at the propagating tip of a continental rift—a geochemical study of primitive alkaline volcanic rocks of the western branch of the East African Rift. *Earth Planet. Sci. Lett.* **284**, 236–248 (2009).
 30. Dawson, J. B. Quaternary kimberlitic volcanism on the Tanzania Craton. *Contrib. Mineral. Petrol.* **116**, 473–485 (1994).
 31. Alvarez, P. Evidence for a Neoproterozoic carbonate ramp on the northern edge of the Central Africa Craton: relations with late Proterozoic intracratonic troughs. *Geol. Rundsch.* **84**, 636–648 (1995).
 32. Crosby, A. G., Fishwick, S. & White, N. Structure and evolution of the intracratonic Congo Basin. *Geochem. Geophys. Geosyst.* **11**, Q06010 (2010).
 33. Kadima, E., Delvaux, D., Sebagenzi, S. N., Tack, L. & Kabeya, S. M. Structure and geological history of the Congo Basin: an integrated interpretation of gravity, magnetic and reflection seismic data. *Basin Res.* **23**, 499–527 (2011).
 34. Hartley, R. W. & Allen, P. A. Interior cratonic basins of Africa: relation to continental break-up and role of mantle convection. *Basin Res.* **6**, 95–113 (1994).
 35. Downey, N. J. & Gurnis, M. Instantaneous dynamics of the cratonic Congo Basin. *J. Geophys. Res.* **114**, B06401 (2009).
 36. Forte, A. M. et al. Joint seismic–geodynamic–mineral physical modeling of African geodynamics: a reconciliation of deep mantle convection with surface geophysical constraints. *Earth Planet. Sci. Lett.* **295**, 329–341 (2010).
 37. Griffin, W. L., Graham, S., O'Reilly, S. Y. & Pearson, N. J. Lithosphere evolution beneath the Kaapvaal Craton. Re–Os systematics of sulfides in mantle-derived peridotites. *Chem. Geol.* **208**, 89–118 (2004).
 38. Capitanio, F. A., Nebel, O. & Cawood, P. A. Thermochemical lithosphere differentiation and the origin of cratonic mantle. *Nature* **588**, 89–94 (2020).
 39. Dang, Z. et al. Weak orogenic lithosphere guides the pattern of plume-triggered supercontinent break-up. *Commun. Earth Environ.* **1**, 51 (2020).
 40. Cooper, C. M., Farrington, R. J. & Miller, M. S. On the destructive tendencies of cratons. *Geology* **49**, 195–200 (2020).
- Publisher's note** Springer Nature remains neutral with regard to jurisdictional claims in published maps and institutional affiliations.
- © The Author(s), under exclusive licence to Springer Nature Limited 2022

Methods

Databases. The initial crustal model was constructed from CRUST1.0⁴¹ and LithoRef18⁴² and allowed to change during the Markov chain Monte Carlo inversion within a prescribed range (see the following). Absolute elevation, surface heat flow, upper mantle geoid anomalies, gravity anomalies and gravity gradients were taken from refs. 42–46, respectively. When the spatial resolution of a dataset was higher than that used in our model ($1^\circ \times 1^\circ$), the original data were spatially averaged within a $1^\circ \times 1^\circ$ cell; the resulting mean values were then used as inputs, and the standard deviations were considered when assigning overall uncertainties (see the following). Note that this measure of spatial variability within a cell is typically larger than the true observational uncertainty of the field. Geoid anomalies reported in ref. 42 (and used here) were filtered to minimize the effects of deep mantle density anomalies that are not considered in the inversion. Observed and predicted gravity gradients were compared at satellite height (250 km).

A complete set of Rayleigh-wave dispersion curves was obtained by supplementing a global dataset⁴⁷ with higher-resolution, regional studies and by ambient noise tomography for periods <50 s in selected regions (Supplementary Figs. 1 and 2). In particular, we used dispersion data from the tomography studies of ref. 48 in South Africa, ref. 49 in Cameroon and ref. 50 in the East African Rift (see Supplementary Information for period ranges and Supplementary Fig. 24 for regions covered by the regional tomography studies^{48–50}). In regions without dispersion data, we computed dispersion curves in the period range 25–160 s at the points of interest from one-dimensional (1D) velocity profiles extracted from the global model of ref. 47. In doing so, we use a modified version of the software *disp96*^{13,51} and the attenuation model of ref. 52. To minimize unwanted artifacts due to truncation effects during the computation of dispersion curves at the longest periods, we extended the velocity-density structure of the mantle from the bottom of the inversion volume (410 km depth) down to 1,500 km depth using the global model of ref. 53. For the ambient noise tomography, we processed data from 870 stations over 25 years of seismic noise recorded by 20 arrays (see Supplementary Information). We used a standard noise cross-correlation technique with a time–frequency phase weighted stacking method to improve the signal-to-noise ratio^{54,55}. Supplementary Fig. 2 shows examples of the resultant dispersion curves and their uncertainties.

We did not consider radial anisotropy in our inversions. Radial anisotropy in the upper mantle causes the vertically polarized shear-wave velocity (VSV) (and the associated Rayleigh-wave phase velocity) to differ from the isotropic average VS_{iso} of the mantle assemblage (for example, $VS_{iso} = (VSV + VSH)/2$; where VSH is the velocity of horizontally polarized shear waves). Horizontally oriented fabrics produce positive radial anisotropy ($VSH > VSV$) whereas vertical fabrics result in negative anisotropy ($VSH < VSV$). This would result in a bias towards higher (lower) temperatures in our model in regions of strong positive (negative) radial anisotropy. The radial anisotropy of the African continent is still subject to large uncertainties, but some studies have shown that it (1) varies within only a few percent laterally, (2) decreases with depth and (3) is generally positive in the first 200 km (refs. 56,57). Although estimating the bias is not straightforward due to the many factors that contribute to the inverted temperature structure, exploratory inversions indicated that the effects of radial anisotropy on our temperature and LAB estimates are well within 1σ of the obtained posterior distributions as long as the average anisotropy in the first 200 km is $\lesssim 3\%$ (Supplementary Fig. 28). In this respect, we note that our temperatures agree well with thermobarometric estimates from the youngest xenoliths in the Kaapvaal and Tanzanian cratons (Supplementary Fig. 29).

Multi-observable probabilistic inversion. All datasets were jointly inverted with a thermodynamically constrained, multi-observable probabilistic inversion method^{11–13}, coded into two Fortran packages: *LitMod1D_4INV* and *LitMod3D_4INV* (<https://www.juanafonso.com/software>). This method is specifically designed to obtain estimates of the physical state (for example, temperature distribution, compositional structure and stress/strain distributions) of the lithosphere and sublithospheric upper mantle by inverting multiple datasets with the necessary complementary sensitivities to the main fields of interest. The inverse problem is cast into a statistical (Bayesian) inference problem^{11,12}. Consequently, the solution to the inverse problem is represented by a multi-dimensional probability distribution (known as the posterior distribution) over the parameters of interest. For parameter estimation problems, the posterior distribution can be written as $\pi(\mathbf{m}) \propto L(\mathbf{m})\rho(\mathbf{m})$, where \mathbf{m} is the vector of model parameters, $\rho(\mathbf{m})$ is the prior distribution describing all the information in the parameter space that is independent from the actual measurements and $L(\mathbf{m})$ is the likelihood function, which describes the probability of obtaining the observed data given \mathbf{m} (a measure of how good the model \mathbf{m} is in explaining the data). Under the assumption of Gaussian uncertainties in the data and model predictions, the likelihood can be written as $L(\mathbf{m}) \propto \exp[-SS(\mathbf{m})]$, where $SS(\mathbf{m})$ is the misfit function that measures the discrepancy between observed and predicted data for all datasets (see the following). Since $\pi(\mathbf{m})$ has no analytical solution, we sample it by constructing a Markov chain that has the posterior distribution as its equilibrium distribution. To do so, we used the Delayed Rejection Adaptive Metropolis algorithm of ref. 58 during the exploratory 1D stage and the Multiple-Try Metropolis algorithm of ref. 59, combined with proposal adaptivity,

during the 3D refinement stage (see refs. 11 and 13 for details on the set-up of the two stages). The final inversions were run in the MG3 cluster at Macquarie University and involved 42×10^6 and 10×10^6 simulations for the 1D and 3D stages, respectively.

In contrast to more traditional inversion methods, we invert directly for the main thermodynamic variables temperature, pressure and major-element composition (CaO, FeO, MgO, Al₂O₃ and SiO₂) at specific locations inside our model. More specifically, the mantle is discretized with 20,955 nodes where the full Gibbs free-energy minimization is performed at each Markov chain Monte Carlo iteration using components of the software *Perple_X*⁶⁰ and adopting the thermodynamic model and internally consistent database of ref. 61. This provides the link between the main thermodynamic variables and the physical parameters needed to solve the forward problems (for example, density and bulk modulus) and guarantees that our models will not violate fundamental thermodynamic relations. This is a crucial aspect as the link between bulk density and seismic velocities (and the data sensitivity to these parameters) controls our ability to discriminate between thermal and compositional fields^{10–13}. We do not solve the thermodynamic problem in the crust, where Birch's law is generally obeyed. Instead, we link densities and seismic velocities using the empirical equations in ref. 62. During the inversion, we compute 1D steady-state conductive geotherms in each cell down to the LAB (a model parameter sampled during the inversion), which we identify with the depth to the 1,250 °C isotherm. The geotherm in the sublithospheric mantle is obtained as a linear interpolation between three and six (dependent on the LAB depth) nodes whose temperature is considered unknown and sampled during the inversion. For further details on the method, see refs. 11–13.

Misfit function. Following the arguments in ref. 13, we choose the following form for the misfit function of 2D fields (for example, elevation, gravity anomaly and geoid).

$$SS^j(\mathbf{m}) = \sum_{i=1}^N \frac{(d_i^{\text{calc}} - d_i^{\text{obs}})^2}{\sigma_i^2} \quad (1)$$

where N is the numbers of columns and j is the type of 2D data. For dispersion data, we use

$$SS(\mathbf{m}) = \sum_{i=1}^N \sum_{k=1}^{N_{\text{per}}} \frac{(d_{ik}^{\text{calc}} - d_{ik}^{\text{obs}})^2}{\sigma_{ik}^2} \quad (2)$$

where N_{per} is the number of periods used to represent the dispersion curve. The values of σ come from considering the uncertainties arising from (1) errors in the observed data, (2) averaging data over the area of each $1^\circ \times 1^\circ$ column and (3) errors in the predicted data. In most cases, the last two dominate the final uncertainty^{11,13}. Here we used minimum, yet generous, uncertainties of 150 m for elevation, 5 mGal for gravity anomalies, 0.05 Eötvös for gravity gradients and 1 m for geoid. For Rayleigh-wave phase velocities, we assigned different uncertainties on the basis of the type of data used in specific regions (see Supplementary Figs. 22–25 for examples of data fits). Since the datasets used in this study have different units, uncertainties, data coverage and sensitivities to different aspects of the problem, the simultaneous inversion of these data requires an adequate weighting of each dataset. This avoids solutions that are dominated by one dataset or by nonphysical factors (for example, data density or discretization, inherent incompatibilities between datasets). Therefore, the final misfit is obtained as the weighted sum of all the preceding misfits: $\phi_{\text{total}} = \sum_l w_l SS_l^j$, where l indicates a specific type of dataset. The weights w_l used in the final inversions were chosen on the basis of the performance of ten preliminary inversions.

Data availability

The data that support the findings of this study are available from the community data repository Figshare at <https://doi.org/10.6084/m9.figshare.19322180>.

Code availability

The codes used to perform the inversions are available from the corresponding author upon request or via <https://www.juanafonso.com/>.

References

- Laske, G., Master, G., Ma, Z. & Pasyanos, M. Update on CRUST1.0—A 1-degree global model of Earth's crust. *Geophys. Res. Abstr.* **15**, EGU2013–2658 (2013).
- Afonso, J. C., Salajegheh, F., Szwilius, W., Ebbing, J. & Gaina, C. A global reference model of the lithosphere and upper mantle from joint inversion and analysis of multiple data set. *Geophys. J. Int.* **217**, 1602–1628 (2019).
- Amante, C. & Eakins, B. W. *ETOPO11 Arc-Minute Global Relief Model: Procedures, Data Sources and Analysis* NOAA Technical Memorandum NESDIS NGDC-24 (National Geophysical Data Center, NOAA, 2009); <https://doi.org/10.7289/V5C8276M>
- Goutourbe, B., Poort, J., Lucazeau, F. & Raillard, S. Global heat flow trends resolved from multiple geological and geophysical proxies. *Geophys. J. Int.* **187**, 1405–1419 (2011).

45. Bonvalot, S. et al. *World Gravity Map* (International Gravimetric Bureau, 2012).
46. Kvas, A. et al. ITSG-Grace2018: overview and evaluation of a new GRACE-only gravity field time series. *J. Geophys. Res. Solid Earth* **124**, 9332–9344 (2019).
47. Schaeffer, A. J. & Lebedev, S. Global shear speed structure of the upper mantle and transition zone. *Geophys. J. Int.* **194**, 417–449 (2013).
48. Yang, Y., Li, A. & Ritzwoller, M. H. Crustal and uppermost mantle structure in southern Africa revealed from ambient noise and teleseismic tomography. *Geophys. J. Int.* **174**, 235–248 (2008).
49. Adams, A. N. et al. Lithospheric instability and the source of the Cameroon Volcanic Line: evidence from Rayleigh wave phase velocity tomography. *J. Geophys. Res. Solid Earth* **120**, 1708–1727 (2015).
50. O'Donnell, J. P., Adams, A., Nyblade, A. A., Mulibo, G. D. & Tugume, F. The uppermost mantle shear wave velocity structure of eastern Africa from Rayleigh wave tomography: constraints on rift evolution. *Geophys. J. Int.* **194**, 961–978 (2013).
51. Herrmann, R. B. Computer Programs in Seismology v.3.30 <http://www.eas.slu.edu/eqc/eqcsoftware.html> (Saint Louis University, 2002).
52. Dalton, C. A., Ekström, G. & Dziewonski, A. M. The global attenuation structure of the upper mantle. *J. Geophys. Res.* **113**, B09303 (2008).
53. Simmons, N. A., Forte, A. M., Boschi, L. & Grand, S. P. GyPSuM: a joint tomographic model of mantle density and seismic wave speeds. *J. Geophys. Res.* **115**, B12310 (2010).
54. Schimmel, M. & Gallart, J. Frequency-dependent phase coherence for noise suppression in seismic array data. *J. Geophys. Res. Solid Earth* **112**, B04303 (2007).
55. Li, G., Niu, F., Yang, Y. & Xie, J. An investigation of time-frequency domain phase-weighted stacking and its application to phase-velocity extraction from ambient noise's empirical Green's functions. *Geophys. J. Int.* **212**, 1143–1156 (2018).
56. Sebai, A., Stutzmann, E., Montagner, J.-P., Sicilia, D. & Beucler, E. Anisotropic structure of the African upper mantle from Rayleigh and Love wave tomography. *Phys. Earth Planet. Inter.* **155**, 48–62 (2006).
57. Ravenna, M., Lebedev, S., Fullea, J. & Adam, J. M.-C. Shear-wave velocity structure of southern Africa's lithosphere: variations in the thickness and composition of cratons and their effect on topography. *Geochem. Geophys. Geosyst.* **19**, 1499–1518 (2018).
58. Haario, H., Laine, M., Mira, A. & Saksman, E. DRAM: efficient adaptive MCMC. *Stat. Comput.* **16**, 339–354 (2006).
59. Liu, J. S., Liang, F. & Wong, W. H. The multiple-try method and local optimization in Metropolis sampling. *J. Am. Stat. Assoc.* **95**, 121–134 (2000).
60. Connolly, J. A. The geodynamic equation of state: what and how. *Geochem. Geophys. Geosyst.* **10**, Q10014 (2009).
61. Stixrude, L. & Lithgow-Bertelloni, C. Thermodynamics of mantle minerals-II. Phase equilibria. *Geophys. J. Int.* **184**, 1180–1213 (2011).
62. Brocher, T. M. Empirical relations between elastic wavespeeds and density in the Earth's crust. *Bull. Seismol. Soc. Am.* **95**, 2081–2092 (2005).

Acknowledgements

We thank S. Lebedev for valuable suggestions. We also acknowledge the AfricaArray programme and all its members. W.B.-M. and J.C.A. acknowledge funding from ARC Grant DP160103502, ARC CE110001017, ARC Linkage Grant LP170100233 and Macquarie University DVCR co-funding scheme. This is contribution 1681 from the ARC Centre of Excellence for Core to Crust Fluid Systems (www.ccfsmq.edu.au) and 1480 in the GEMOC Key Centre (<http://www.gemoc.mq.edu.au>).

Author contributions

J.C.A., N.J., A.M. and W.B.-M. conceived the project. W.B.-M., J.C.A., E.S. and I.F. performed the inversions and processed all datasets and results. All authors analysed the results and contributed to writing the manuscript.

Competing interests

The authors declare no competing interests.

Additional information

Supplementary information The online version contains supplementary material available at <https://doi.org/10.1038/s41561-022-00929-y>.

Correspondence and requests for materials should be addressed to Juan C. Afonso.

Peer review information *Nature Geoscience* thanks Sergei Lebedev, Atalay Ayele and the other, anonymous, reviewer(s) for their contribution to the peer review of this work. Primary Handling Editor: Rebecca Neely, in collaboration with the *Nature Geoscience* team.

Reprints and permissions information is available at www.nature.com/reprints.